Experimental investigation of shock induced panel flutter with simultaneous use of DIC and PIV

A. D'Aguanno[1,*], P. Quesada Allerhand[1], F.F.J. Schrijer[1], B.W. van Oudheusden[1]

1: Aerodynamics Section, Delft University of Technology, Netherlands
*Corresponding author: a.daguanno@tudelft.nl

Keywords: Fluid-structure interaction, SWBLI, panel flutter, PIV, DIC

ABSTRACT

In this experimental study, both classical and shock induced supersonic panel flutter are investigated at a freestream Mach number of 2, using a combination of planar particle image velocimetry (PIV) and stereographic digital image correlation (DIC) to obtain simultaneous full-field structural displacement and flow velocity measurements. High-speed cameras are employed to obtain a time-resolved description of the panel motion and of the flow dynamics. In order to prevent interference between the PIV and DIC systems, an optical isolation is implemented using fluorescent paint, dedicated light sources, and camera lens filters. For the shock induced case, the effect of the panel motion on the SWBLI behavior is assessed, by comparing it with the SWBLI on a rigid wall. The results show that panel oscillations occur with an amplitude of ten times the panel thickness. The dominant frequencies observed in the panel oscillation (424 Hz and 1354 Hz) match the main spectral content of the reflected shockwave position. In absence of shock impingement, the oscillation amplitude is on the order of the panel thickness, while the dominant frequency contribution is at 730 Hz.

The fluid-structure coupling is studied by identifying the flow regions of maximum correlation between the panel displacement and the flow velocity fluctuations. In presence of shock impingement the results obtained proved that the inviscid flow region upstream of the SWBLI is perfectly in phase with the panel oscillation, while the downstream region has a delay of one quarter of the flutter cycle. Instead, no delay is observed for the configuration in absence of shockwave impingement.

1. Introduction

The vibration of thin structural surface elements exposed to a supersonic flow represents a fluid-structure interaction (FSI) phenomenon that can seriously affect the performance and structural integrity of supersonic aircraft and spacecraft systems. This is, for example, the case of the X-15 aircraft, which experienced flutter on both fairing and tail panels (Kordes et al. (1960)). These adverse effects are further amplified when a shockwave/boundary-layer interaction (SWBLI) occurs over the panel, since the increased pressure and thermal loads on the panel further compromise

the strength and stiffness of the plate (Spottswood et al. (2019)). Panel flutter induced by a SWBLI has been observed for a multitude of high-speed vehicles such as the X-15 (Dowell & Bendiksen (2010)) or in the operation of a non-adaptable exhaust nozzle (like that of a launch vehicle) during the start-up. The accompanying over-expanded flow can lead to shockwave boundary layer interaction on the flexible nozzle wall, where impinging oblique shocks trigger violent oscillations of the nozzle (Pasquariello (2018), Garelli et al. (2010)). A better understanding of this phenomenon, which is generally referred to as shock-induced panel flutter (Boyer et al. (2018)), is therefore crucial for the design of future high-speed vehicles. The characteristics of SWBLIs induced by an oblique shockwave in the presence of a rigid surface has received extensive attention. The main flow features are sketched in Fig.1 (left), while a more detailed description can be found in reference texts, such as the one given by Babinsky & Harvey (2011).

Classical supersonic panel flutter has been extensively studied in literature, with Dowell (1975) presenting an overview of the theoretical models and the physical aspects of flutter, whilst Mei et al. (1999) has given a general review of the most relevant results on panel flutter in the last century. A more recent review is provided by Dowell & Bendiksen (2010), which also studies viscosity effects. On the other hand, several numerical studies have approached shock-induced panel flutter in recent years such as Visbal (2012) (with compressible Euler equations coupled with the von Karman plate equation), Pasquariello et al. (2015) (which used LES) and Shinde et al. (2018) (where 3D effects are also taken into account). The use of numerical simulations has the attractive feature (when compared to experiments) of providing complete flow characterization data with a high spatial and temporal resolution, and with the opportunity of conveniently changing the main parameters at will. However, (high-fidelity) numerical simulations are also restricted by issues, such as the limited Reynolds number and the limited computational domain. For this reason validating experiments remain valuable.

In a typical panel flutter experiment, a flat (or curved) plate is assembled in the wind tunnel test section and the dynamic pressure of the wind tunnel is increased until flutter is achieved. Many experimental studies in the past were focused on determining the effects of different geometry, flow and boundary conditions on the flutter boundaries. Anderson (1962) determined the flutter boundaries of flat and curved plates at a Mach number of 2.81 using inductance pickups to measure the plate vibration. Dowell & Voss (1965) performed various experiments studying the effect of panel dimensions, panel mechanical properties, Mach number, and acoustic cavity size on flutter boundaries using vibrometers, strain gauges and thermocouples. In these experiments only a limited characterization of the flow was performed, typically providing only freestream Mach number and dynamic pressure. The experimental techniques as used in these previous studies further allow only single point measurements of the flow and the plate displacement, whereas computational simulations allow a full-field analysis of both the plate motion and the surrounding flow. To provide complimentary full flow-field experimental data, more advanced measurement techniques, such as particle image velocimetry (PIV), should be incorporated. Very few experimental studies using full flow-field techniques have been used to investigate shock induced panel flutter. On the other hand, these techniques have already been extensively used under similar

conditions for the study of a shockwave impinging on a rigid plate as documented in the review paper of Clemens & Narayanaswamy (2014). SWBLI induced by an impinging oblique shockwave is described by Humble et al. (2007) using planar PIV. In a following study van Oudheusden et al. (2011) used high-speed PIV to measure the time-resolved 2D flow of a SWBLI and to study the associated flow unsteadiness. Piponniau et al. (2009) has used PIV data to verify a model which explains the low-frequency unsteadiness for cases in which the flow is reattaching downstream of the impinging shockwave. Furthermore, Schreyer et al. (2015) studied SWBLI using a dual PIV system (multi-exposure) to simultaneously achieve a sufficiently high spatial and temporal resolution.

Regarding the experimental characterization of the shock-induced panel flutter itself, Spottswood

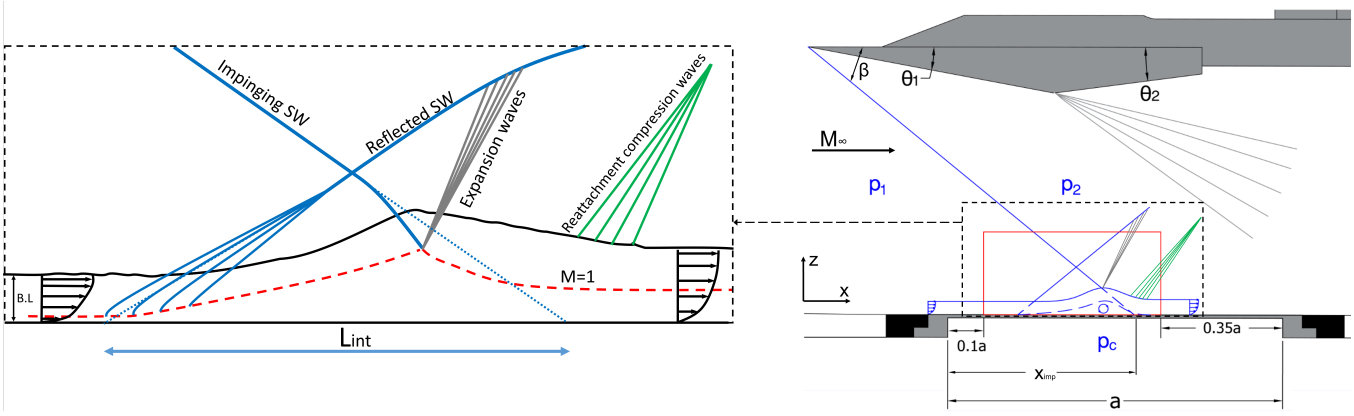

Figure 1. Schematic overview of the SWBLI developing on a rigid panel (left). On the right sketch of the experimental geometry, including the PIV FOV outlined in red (side-view).

et al. (2012) used high-speed digital image correlation (DIC) to achieve a detailed measurement of the vibration response of a thin plate during shock-induced panel flutter. The use of DIC provided a complete description of the plate displacement, which allowed the extraction of the panel vibration mode shapes. Pressure sensitive paint (PSP) was used to quantify the pressure distribution on the plate surface even if no accompanying flow field measurements were performed. Similarly to the previous study, in Spottswood et al. (2019) DIC was employed to record the panel movement from both the cavity and the flow side, without noticing relevant differences. Recently, Brouwer et al. (2021) conducted full field DIC measurements of a thermally buckled panel. Further panel flutter investigation employing PSP measurements have been, conducted by Tripathi et al. (2021). To the best of the authors' knowledge, Tripathi et al. (2021) is also the only study in which also PIV was employed for studying this phenomenon.

Moreover, no experimental studies on shock induced panel flutter have been reported so far, which employ both DIC and PIV in combination. In contrast, the measurement of both flow and structure using PIV and DIC simultaneously has been documented for low speed fluid-structure interactions, as in Zhang & Porfiri (2019)), which proves the feasibility of the simultaneous use of these techniques. Hortensius et al. (2018) is the only study in which these techniques have been used under supersonic conditions, particularly for studying the interaction between an underexpanded jet and an adjacent compliant surface, without time resolving neither the flow nor the structure.

The objective of the current study is to experimentally investigate classical and shock induced panel flutter using PIV and DIC simultaneously, with the aim of assessing the feasibility of using these selected techniques for this particular fluid-structure interaction, and generating reliable full-field experimental data. The tests have been conducted on a panel with free side edges, for which a nominally 2D flutter response is predicted, from both the flow and structural perspective.

2. Experimental procedures

2.1. ST-15 wind tunnel

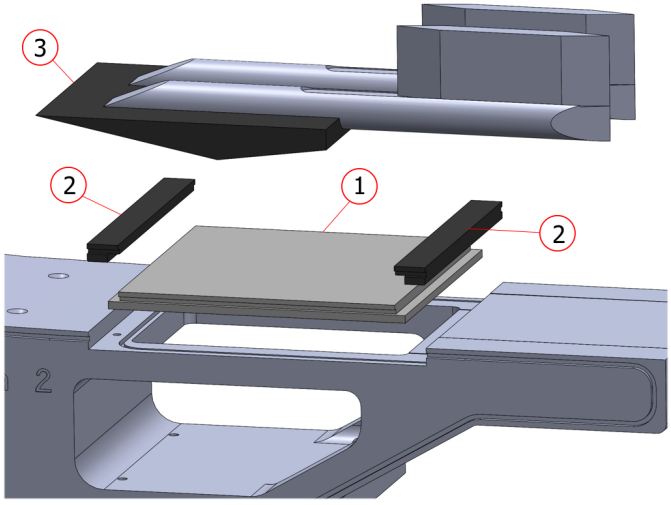

Figure 2. Technical drawing of ST-15 (left) and 3D CAD rendering of the test section (right) with panel (1), clamping pieces (2) and shock generator (3).

The tests have been performed in the ST-15 supersonic blowdown wind tunnel of TU Delft. The tunnel is equipped with interchangeable nozzle blocks, that form the top and bottom walls. For this study a Ma = 2 configuration was used. The rectangular test section has a size of 15cm x 15cm x 25cm (height x width x length) with two side windows (diameter of 250 mm) allowing optical access to the test section.

The wind tunnel was operated at a total pressure $p_0 = 2.5$ bar and total temperature $T_0 = 288K$. For these stagnation conditions and a free stream Mach number $Ma_\infty = 2$, the corresponding dynamic pressure is $q_\infty = 0.89$ bar. The boundary layer thickness at the entry of the test section is $\delta_{99,0} = 5.2$ mm (Giepman et al. (2018)). The main operational parameters have been summarized in Table. 1.

Table 1. Flow conditions

Parameter	Symbol	Value	Unit
Free stream Mach number	Ma_∞	2	
Free stream velocity	U_∞	442	m/s
Total pressure	p_0	2.5	bar
Total temperature	T_0	288	K
Dynamic pressure	q_∞	0.89	bar
Boundary layer thickness	$\delta_{99,0}$	5.2	mm
Incompressible momentum thickness	θ_i	0.52	mm
Reynolds number per unit length	Re_∞/L	$3.3 \cdot 10^7$	1/m
Reynolds based on θ_i	Re_{θ_i}	$1.5 \cdot 10^4$	-

2.2. Panels

In addition to the tests on the flexible thin panel, additional measurements with a rigid plate were conducted as a baseline reference case.
The thin flexible and rigid panels were made in Al7075-T6 and installed in the lower Mach block by means of two L-shaped clamping pieces, see Fig.2. The figure also shows the presence of the cavity underneath the panels, which is directly connected to the exit of the test section. As such the pressure in the cavity during the experiments was not explicitly controlled.
The thin panel has a thickness $h = 0.3$ mm, length $a = 128$ mm and a span $b = 84$ mm, resulting in an aspect ratio $a/b = 1.5$. The panel is clamped at the leading edge and trailing edge while it is free on its sides as shown in Fig.3 (left). This clamping condition is achieved with two streamwise oriented cuts of 0.2 mm of width. As the rigid baseline case a 9 mm thick solid panel was used, without side slots (see a picture of the rigid panel in Fig.3, right).
For the shock impingement configuration, a shock generator with an angle $\theta_1 = 11^\circ$ was mounted, to create an oblique shockwave impinging at $x_{imp}/a = 0.55$ on the test panel. To reduce the height of the shock generator, and hence its blockage of the flow, it features a second ramp angle ($\theta_2 = 7.8^\circ$) at the rear part (see Fig.2). This causes the formation of expansion waves, which impinge on the bottom wall of the test section, sufficiently far downstream of the flexible panel to not affect the flutter behavior (see Fig.1, right). In Table 2 the most important panel and shock generator parameters are summarized.

2.3. Measurement techniques

For the DIC acquisition, two Photron FASTCAM SA1 high speed cameras have been used in a stereographic configuration. The cameras have been placed at one side of the wind tunnel as indicated in Fig.4 (left). The angle between the two cameras is approximately 45°, which is the optimum value to measure out-of-plane displacements (see Sutton et al. (2009)). The orientation of the cameras with respect to the measurement plane is shown in Fig.4 (right) with the 2 DIC

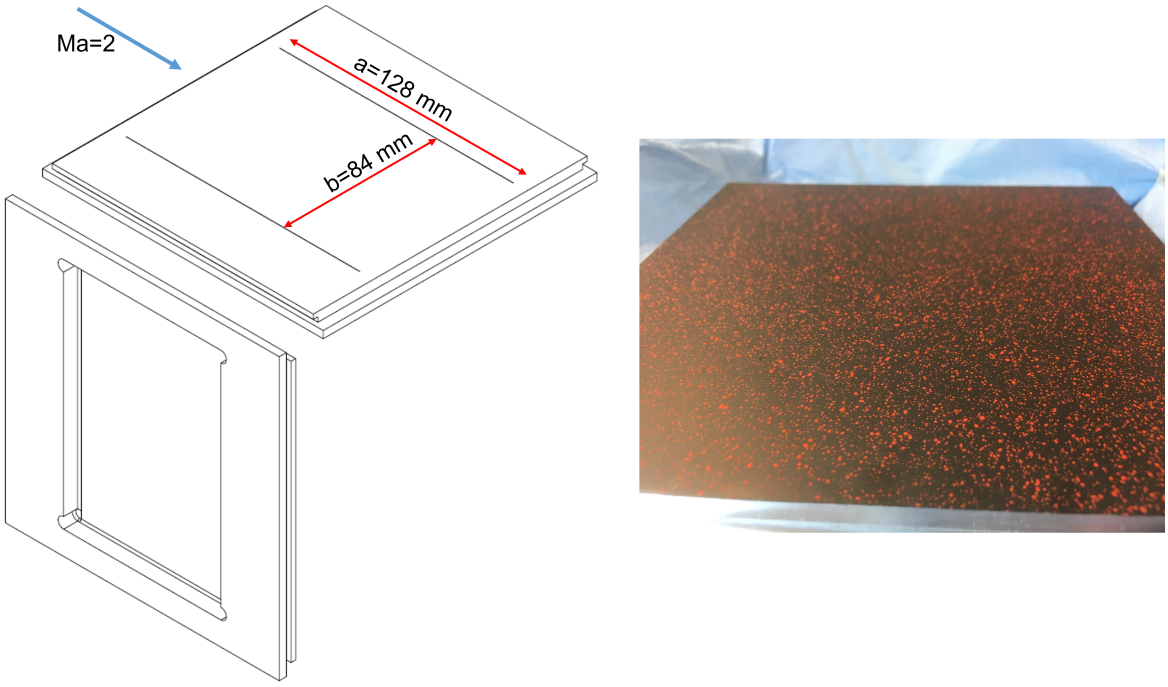

Figure 3. Technical drawing of flexible panel (left). On the right, rigid panel with speckle pattern on it.

cameras having a symmetrical position with respect to the vertical plane passing for x/a=0.5. Both Photron cameras were operated at an acquisition frequency of 5000 Hz and with a full resolution of $1024px \times 1024px$. The acquisition frequency has been selected such as to obtain time resolved measurements with respect to the most energetic panel flutter frequencies. Each camera was equipped with a 105 mm Nikkor objective with $f_{\#} = 11$ and Scheimpflug adapter to align the focal plane of the cameras with the non-deformed surface of the panel. The resulting depth of focus was approximately 16 mm which was sufficient to keep the plate in focus when deformed during the measurements. The resulting DIC FOV is approximately 120 mm long and 100 mm wide, thus covering the entire panel (except for small regions at the LE and TE of the panel).
The DIC cameras image the movement of the panel by tracking a speckle pattern on the surface

Table 2. Model parameters

Parameter	Symbol	Value	Unit
Length panel	a	128	mm
Span panel	b	84	mm
Thickness panels	h	0.3	mm
Angle shock generator	θ_1	11	°
Second ramp angle	θ_2	7.8	°
Impinging shock angle	β	40.4	°
SW impinging point	x_{imp}/a	0.55	-
Pressure ratio across impinging SW	p_2/p_1	1.8	-

of the panel. The pattern consisted of air brushed dots of fluorescent paint (from LaVision) with an imaged size ranging from 3 to 7 pixels. In order to have a good contrast between the black background of the panel and the fluorescent paint, a speckle coverage of nearly 50% of the panel surface was used (see Fig.3, right). In order to acquire images of the speckle pattern at such a high frequency a blue LED lamp was used which was installed between both cameras (see Fig.4). The LED was synchronized with the DIC cameras by means of a high speed controller with a pulse time $\tau_{LED} = 20\ \mu s$. The synchronization mechanism is described in more details in Section 2.4.

The flow field in the center streamwise plane, over the panel, was measured by means of two-

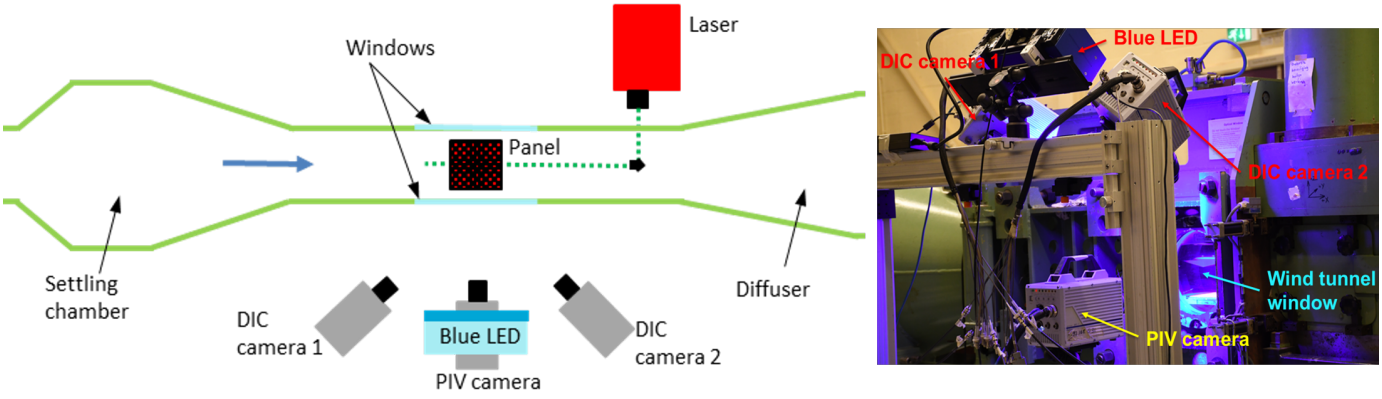

Figure 4. On the left sketch of optical measurement set-up (top-view), while on the right picture of the set-up showing the cameras arrangement.

component particle image velocimetry. A single camera in planar configuration was employed, acquiring images in a chordwise-vertical oriented plane of measurement passing along the mid-span of the panel, as clarified in Figs. 1 (right) and 4. Since the PIV and DIC systems are synchronized, the acquisition frequency was 5000 Hz for the PIV recording as well. In total 4719 image pairs were acquired in double pulse mode with an interframe time of $dt = 2\mu s$. The camera was fitted with a lens with a focal length of 105mm with $f_{\#} = 4$. These settings were combined with a cropped sensor resolution of $1024px \times 592px$ with the PIV FOV extending longitudinally from $x/a = 0.1$ to $x/a = 0.65$ (with the origin of the x-axis corresponding to the leading edge of the panel), and vertically from $z/a = 0$ to $z/a = 0.25$ (see Fig.1, right) this FOV was selected so as to include the main flow features developing on the panel, namely the reflected and impinging shockwave, the separated area as well as the expansion waves developing downstream of the interaction between the impinging shockwaves and separated area.

DEHS particles were used as flow tracers, which have a relaxation time $\tau_p = 2\mu s$ and a particle diameter $d_p \approx 1\mu m$ (see Ragni et al. (2011) for more details). The seeding particles were illuminated by a Nd:YAG Continuum MESA PIV dual cavity laser. By means of an optical probe, a 1mm thick laser sheet passing along the mid-span of the panel is achieved.

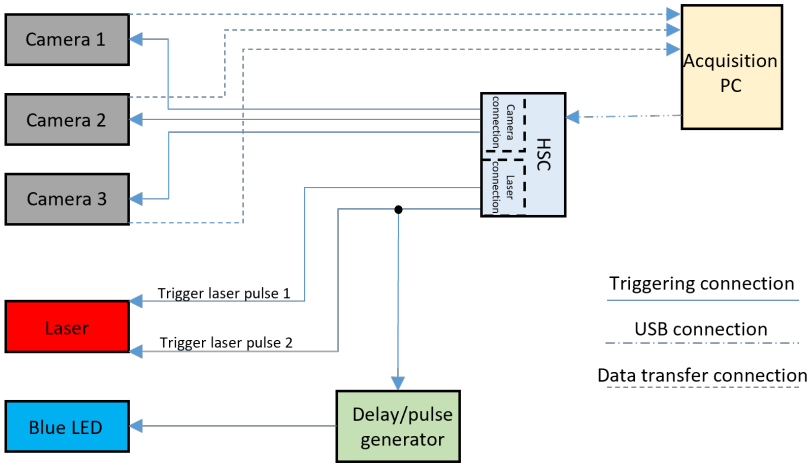

Figure 5. Connection diagram

2.4. Synchronisation and optical isolation

The synchronisation of the three cameras (two for DIC and one for PIV) and the laser pulses was achieved with a high-speed controller (HSC) from LaVision. The trigger of the LED was then connected to the trigger of the second laser pulse such that they would be triggered at the same time. A digital delay/pulse generator was connected between the LED and the second laser pulse trigger to control the pulse duration of the LED which was set equal to 20 μs. A simplified schematic of the connection diagram which highlights the hardware present in the set-up is shown in Fig.5.
Because of the simultaneity of the PIV and the DIC measurements it has been necessary to have an optical isolation between the two systems, which has been accomplished by using: a blue illumination for the LED light; an orange fluorescent paint for the DIC speckle pattern; a bandpass filter for the PIV camera; a highpass filter for the DIC cameras; a PIV laser with a wavelength of $\lambda = 532\ nm$.
A graphical representation of this optical isolation system is shown in Fig. 6, indicating the emission wavelength spectra of the light sources and of the fluorescent paint and the transmitted wavelength spectra of the camera optical filters. The orange fluorescent paint for the speckle pattern has been selected such that when it is illuminated by the blue LED light ($\lambda_{LED} \sim 420 - 500\ nm$), it reemits at higher wavelengths than the laser ($\lambda_{paint} \sim 600 - 750\ nm$). To ensure that the DIC acquisition is not influenced by the PIV illumination system and vice versa, optical filters have been fitted on all the camera lenses. For the DIC cameras, longpass filters have been employed with a cut-off wavelength $\lambda_{cut} = 580\ nm$, to avoid any illumination from the laser. Similarly on the PIV camera a bandpass filter ($\lambda_{band} \sim 475 - 575\ nm$) has been used to avoid illumination from both the blue LED and the fluorescent paint.
The effect of the highpass filters on the DIC performance is demonstrated in Fig.7, which shows the raw DIC images both in presence and in absence of filters. Both images have been acquired in presence of PIV seeding illuminated by the PIV laser light. In the image on the left, the presence of the laser sheet, makes the evaluation of the panel displacement field near the mid-span unreliable.

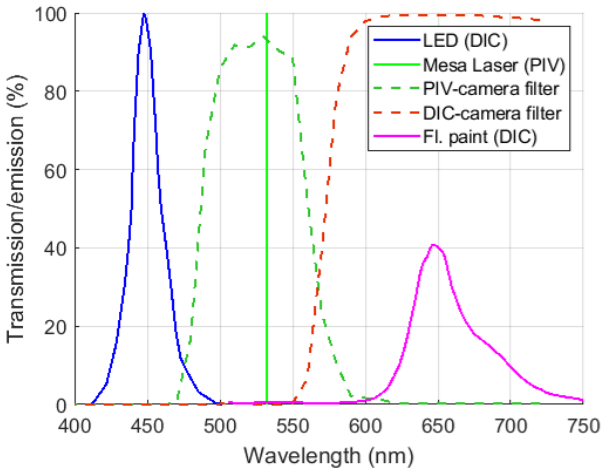

Figure 6. Optical Isolation.

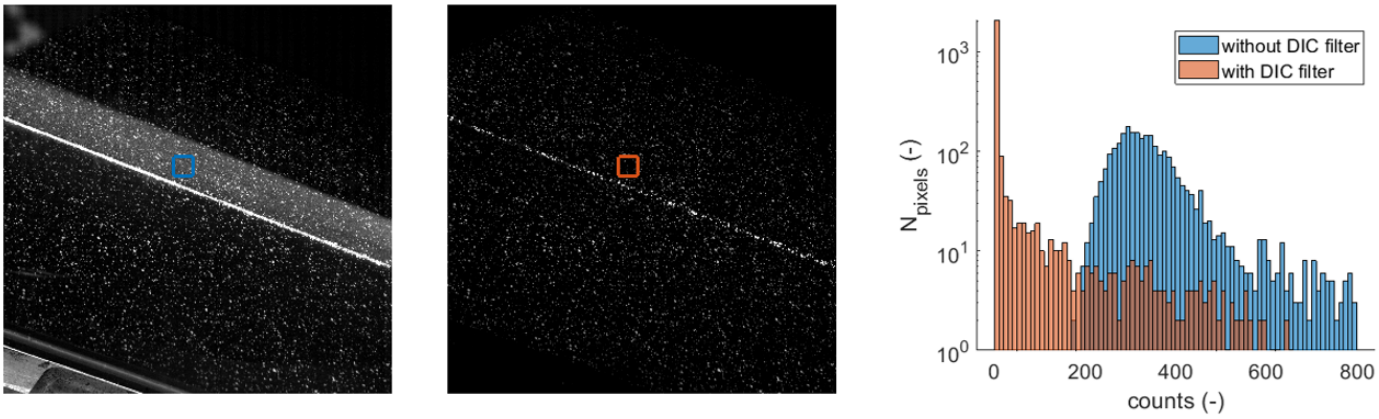

Figure 7. Comparison of DIC raw images with (center) and without (left) highpass filter. On the right an histogram shows the image counts distribution for two square regions (blue on the left image and orange in the center) belonging to the two DIC raw images.

The use of the DIC camera filter (center image) prevents this effect, with only a small contribution of laser reflections on the surface remaining. To quantify this aspect, a histogram of the pixel intensity is shown for two square regions (indicated in the images by the blue and orange squares) of $50px \times 50px$ of the two DIC raw images (see Fig.7). The histogram for the image without DIC filter, reveals that due to the laser illumination, no pixel intensity values below 200 counts occur. In contrast, with the highpass filter applied, an optimal contrast is regained between the black background and the intensity counts of the speckle pattern.

Also for the bandpass filter used for the PIV camera the histograms of the pixel intensity were determined (see Fig.8) for the two configurations (with and without filter) in two square regions of $50px \times 50px$ each. The corresponding distributions reveal that the effect of the filter is that of shifting the entire distribution to lower counts of pixel intensity.

However, although the bandpass filter helps to minimize the reflections on the wall of the panel due to the LED, it was found that it has only a marginal contribution on the evaluation of the velocity vectors. This observation is associated with the fact that, even without the PIV filter, the DIC

light is not able to sufficiently illuminate the seeding particles.

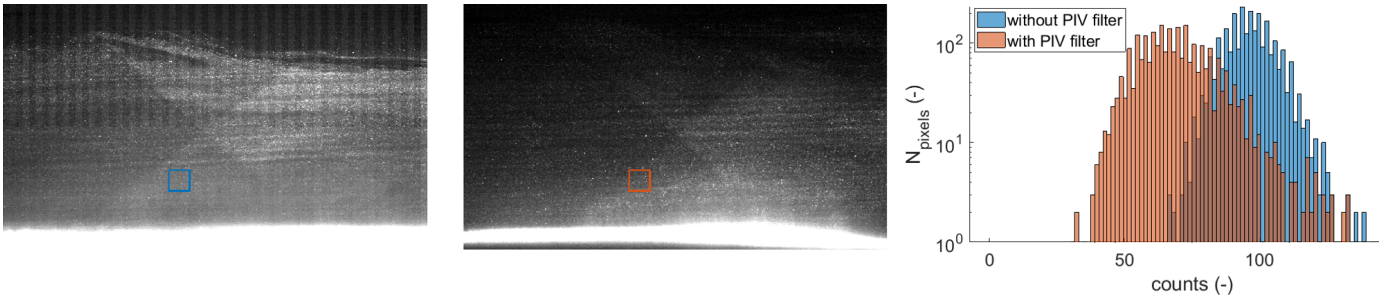

Figure 8. Comparison of PIV raw images with (center) and without (left) bandpass filter. On the right the histogram shows the image counts distribution for the indicated two square regions (blue on the left image and orange in the center) for the two PIV raw images.

2.5. Mutual effect of PIV and DIC

Notwithstanding the application of optical filters on both the PIV and the DIC cameras to separate the two measurement systems, it was verified whether the PIV measurements had a remaining effect on the DIC measurements and vice versa.
To analyze the effect of the PIV laser illumination on the DIC measurement in a quantitative manner, the standard deviation of the vertical displacement field is shown in Fig.9 both in presence (right) and in absence (left) of the simultaneous PIV measurement. To isolate this effect and to avoid any secondary contribution (panel movement and aberration effect) the data are reported for the rigid panel in absence of shock impingement. The results highlight that outliers occur only in correspondence of the laser sheet location (dashed green line) in presence of the simultaneous PIV measurement. However, the magnitude of the corresponding standard deviation is very small ($z_{Std}/h = 4.5 \cdot 10^{-3}$) and comparable with the noise level in absence of laser illumination ($z_{Std}/h = 2.5 \cdot 10^{-3}$). Furthermore the additional noise contribution is negligible with respect to the flutter amplitude of the flexible panel which with and without shock impingement is respectively in the order of $z_{Std}/h = 2.1$ and $z_{Std}/h = 0.3$, as will be discussed in the following sections.

A similar procedure was also carried out to qualitatively visualize the contribution of the DIC system on the PIV measurements. In this case the standard deviation of the streamwise velocity component for the rigid panel in absence of shock impingement is considered as a comparison metric. In presence of the simultaneous DIC measurement, a relatively low increase of fluctuation in the velocity field is observed, in particular, close to the surface of the panel (from $V_{x_{Std}}/V_\infty \approx 0.06$ to $V_{x_{Std}}/V_\infty \approx 0.10$ in presence of DIC). It should be pointed out that another aspect that affects the standard deviation of the velocity field is the variability of the seeding, which could further affect the comparison of the two cases. It is also worth commenting that in both cases a slight increase of standard deviation is observed for $z/a < 0.05$, which is approximately the boundary layer region ($\delta \approx 5.2mm$).

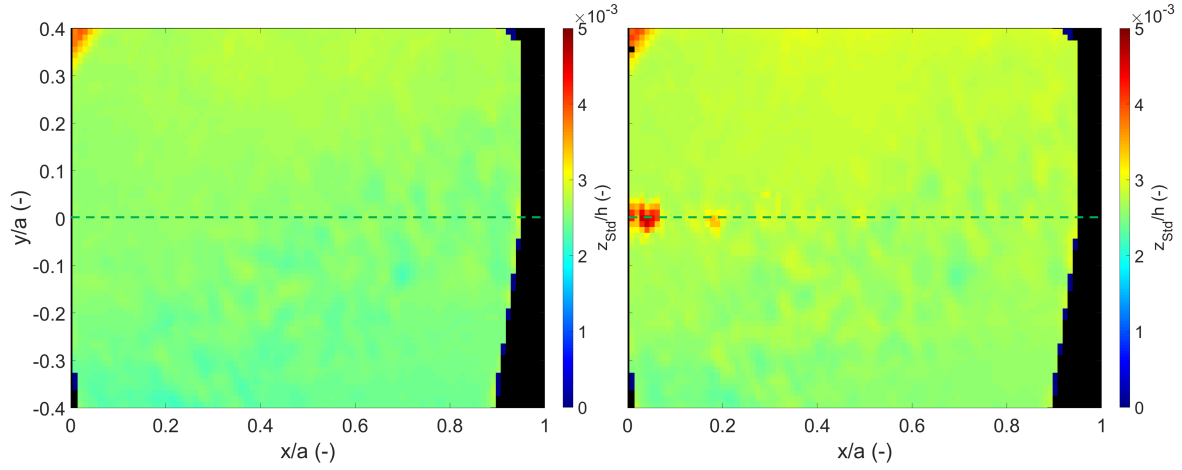

Figure 9. Effect of PIV on DIC measurements. The standard deviation of the displacement field on the rigid panel (without shock impingement) is shown both with (right) and without (left) simultaneous PIV measurement. The dashed green line indicates the laser sheet location.

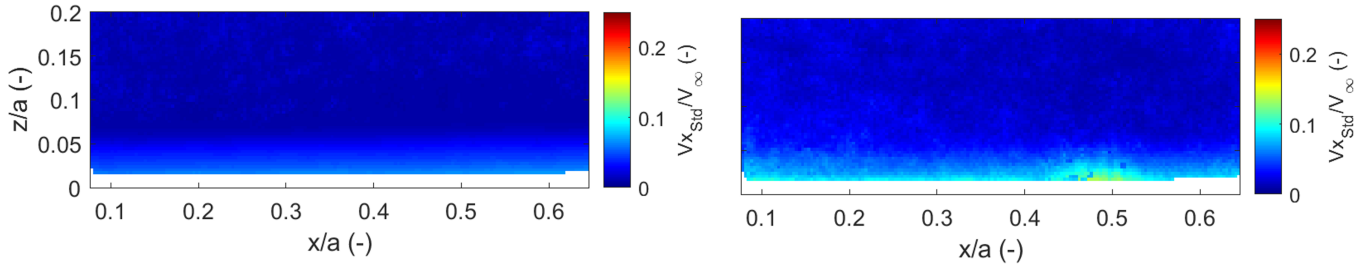

Figure 10. Effect of DIC on PIV measurements. The standard deviation of the streamwise velocity field on the rigid panel (without shock impingement) is shown both with (right) and without (left) simultaneous DIC measurement.

2.6. Data Processing

As it is clear from Fig.8, the raw PIV snapshots suffer from significant laser light reflections from the surface of the panel. Therefore, the images were pre-processed by means of a Butterworth time filter having a length of seven images (Sciacchitano & Scarano (2014)). In addition, the region in which the panel was oscillating was completely masked to avoid the occurrence of outliers in proximity of the surface of the panel. Thus, the vertical extent of the field of view in which velocity vectors are obtained is limited to ranging from $z/a = 0.032$ to $z/a = 0.25$ (the latter being the original upper boundary of the FOV, see Section 2.3). The velocity vectors were subsequently obtained from a multi-pass cross-correlation analysis with a window size of $96px \times 96px$ and three additional passes with a circular window size of $24px \times 24px$. The overlap was set to 75% which results in a final vector spacing of $\Delta x_{PIV}/a = 0.38mm$ corresponding to $\Delta x_{PIV}/a = 0.003$.
For the DIC data, the displacement field has been evaluated with a cross-correlation procedure, in which each instantaneous raw image is correlated with a reference image, obtained as the average of 100 images of the panel that were taken in absence of flow (static panel position). A window (subset) size of $39px \times 39px$ with an overlap of 66% has been used, which results in a vector spacing of $\Delta x_{DIC}/a = 0.011$. The cross-correlation is limited to estimate only average translational dis-

placement per interrogation window, without taking into account complex rotation, which could cause the subset pair of one image to differ greatly from the reference image (Sutton et al. (2009)). To minimize these differences a least squares matching method is used to map the intensity field of the reference image into coordinates of the instantaneous raw image of the deforming panel.
A summary of the main DIC and PIV settings is reported in Table 3.

Table 3. DIC and PIV settings

Setting	DIC	PIV
Acquisition frequency	5 kHz	5 kHz
Number of images	4719	4719 (pairs)
Final resolution	1024×1024 px	1024×592 px
Field of view (x/a)	0.04 - 0.98	0.10 - 0.65
Vector spacing (Δx)	1.40 mm (0.011% a)	0.38 mm (0.003% a)
Final window size	39×39 px (4.22×4.22 mm)	24×24 px (1.54×1.54 mm)
Window overlap	66%	75%

2.7. Uncertainty analysis

The main sources of uncertainty for both the DIC and PIV techniques are discussed below, with the estimated values collected in Table. 4.
For the PIV data the highest source of uncertainty on the velocity value is the uncertainty caused by the particle slip. This uncertainty is caused by the effect that the tracer particles do not perfectly follow the flow in presence of accelerations induced by strong pressure gradients (as notably introduced by shockwaves). This slip can be quantified in terms of the particle relaxation time, which is $\tau_p = 2$ μs in this case. The magnitude of this uncertainty is very significant in the region near a shockwave ($\epsilon_{slip} < 53.36\ m/s$), however, it can be considered negligible in the remaining FOV.
To verify the accuracy of the experimental procedures, the statistical uncertainty is also computed in regions of the flow and of the panel where virtually no fluctuations are expected. Therefore, for the displacement, the statistical uncertainty is computed by analysis of the rigid panel, yielding $\epsilon_z < 0.19 \times 10^{-3}\ mm$. For the flow velocity the uncertainty is computed for the PIV measurements in the supersonic free stream region upstream of the impinging shockwave, yielding values of $\epsilon_u < 0.25\ m/s$ and $\epsilon_v < 0.21\ m/s$, respectively for the horizontal and vertical component.

Table 4. Uncertainty errors

Uncertainty source	Technique	Value	Unit
Statistical ϵ_u	PIV	< 0.25	m/s
Statistical ϵ_v	PIV	< 0.21	m/s
Statistical ϵ_z	DIC	< 0.19	μm
Cross-correlation ϵ_{cc}	PIV	< 3.42	m/s
Particle slip ϵ_{slip}	PIV	< 53.36	m/s
Spatial resolution (interrogation window size)	PIV	< 1.67	mm
Spatial resolution (subset size)	DIC	< 4.57	mm

3. Main statistics

3.1. Panel without shock impingement

In Fig. 11 the average and standard deviation of the vertical displacement fields are shown for the flexible panel in absence of shockwave impingement. First of all, the average displacement field shows good coherence along the span, with small variations being present only in proximity of the panel side edges. The average displacement field suggests that there is a relevant difference in pressure between the cavity and the region above the panel, with the panel having a positive vertical deformation, with a peak value for $x/a \approx 0.5$. In view of the boundary conditions the displacement field gradually goes to zero in proximity of both the leading edge and the trailing edge of the panel. The standard deviation field highlights the presence of a first bending mode behavior, with maximum intensity in correspondence of the center of the panel. The peak values of standard deviation also suggest that the variation in pressure induced by the panel oscillation is small when compared to the average pressure difference across the panel.

In Fig.12 both the streamwise and the vertical average velocity fields are shown. The plots high-

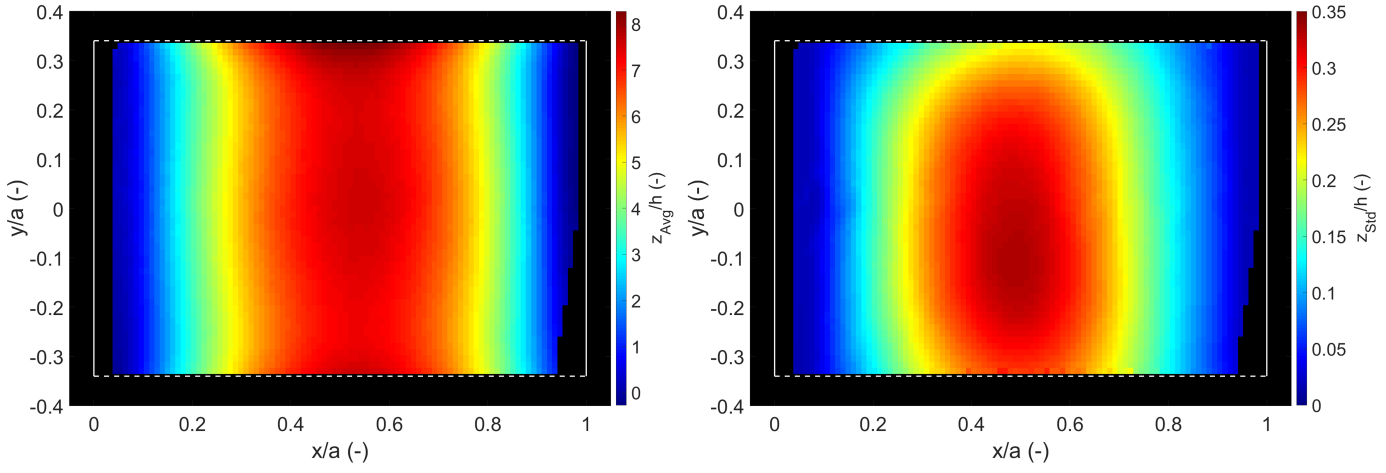

Figure 11. Average (left) and standard deviation (right) of the displacement of the panel without shock impingement.

light the presence of a compression wave, coming from the leading edge of the panel, confirming a permanent positive deformation of the panel at this location.
Because of this deformation, the velocity field experiences positive vertical velocities up to the center of the panel. In accordance with the expansion theory, the flow re-accelerates around $x/a \approx 0.35$, in correspondence of the inflection point of the panel deformation shape. In addition to these flow features, a developing boundary layer is visualized for $z/a < 0.6$, with its size increasing in the streamwise direction.

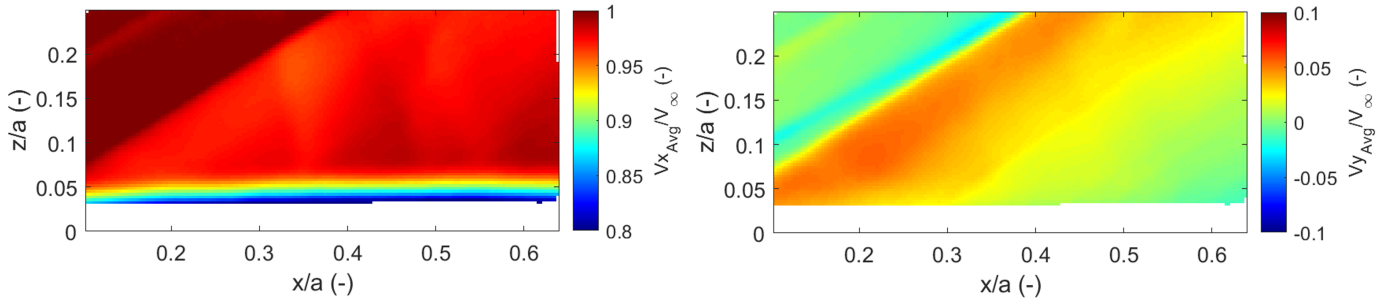

Figure 12. Average horizontal (left) and vertical (right) velocity fields without shockwave impingement.

3.2. Panel with shock impingement

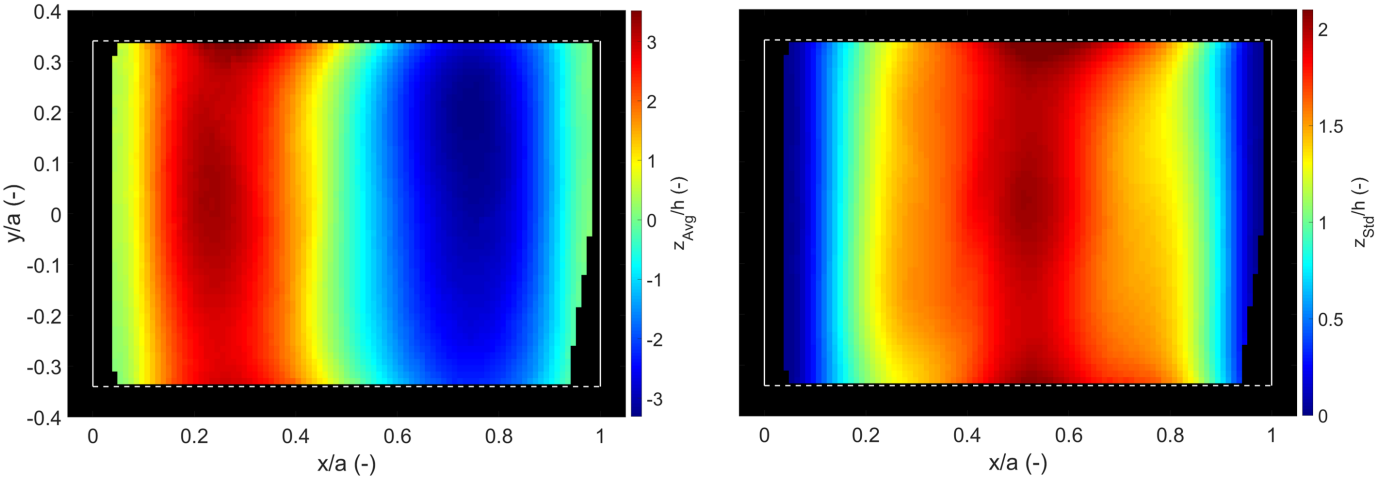

Figure 13. Average (left) and standard deviation (right) of the displacement of the panel with shock impingement.

In Fig. 13 the average and standard deviation of the vertical displacement fields of the flexible panel are shown for the shockwave impingement case. The profile of the average displacement field along the streamwise direction is very different from the non-shockwave case and has a sinusoidal shape (second bending mode) which is induced by the average pressure difference between the upper and lower side of the panel. The pressure on the upper surface of the panel is lower upstream of the interaction region and increases downstream, when passing through the interaction

region, while the pressure in the cavity is expected to be constant. This deformation behavior was also reported by Visbal (2014) and Shinde et al. (2019), but differs from a typical first bending mode shape (with downward deflection) reported by Willems et al. (2013), for the average deflection of the panel. This behavior may be associated with a difference in the cavity pressure.

The strength of the panel oscillation is characterized by the spatial distribution of the standard deviation of the panel displacement, as shown in Fig. 13 (right). The distribution shows a longitudinal symmetry with respect to the mid-panel location $x/a = 0.5$, having the highest values in the center of the panel ($z_{Std}/h = 2$) and gradually decreasing values when moving towards the leading and trailing edge.

As for the non-shockwave case, the average and the standard deviation are very coherent along the spanwise direction, showing that the plate oscillation is predominantly two-dimensional.

From the average velocity distributions (Fig.14) the main flow features are also observed, namely the impinging shockwave, the separated area induced by the shock impingement (green-blue area) and the resulting reflected shockwave. Furthermore, the results confirm an upward deflection of the outer flow field for $0.25 < x/a < 0.45$ in correspondence to the separated area and a downward deflection of the flow for $x/a > 0.45$. A compression wave appears at the leading edge of the panel as for the configuration without shockwave. As a result of the presence of the leading edge compression wave, a reduction of the streamwise velocity component and an increase of the vertical velocity component (flow deflected upstream) occurs.

The standard deviation of the velocity components (Fig.15), highlights that the regions of higher

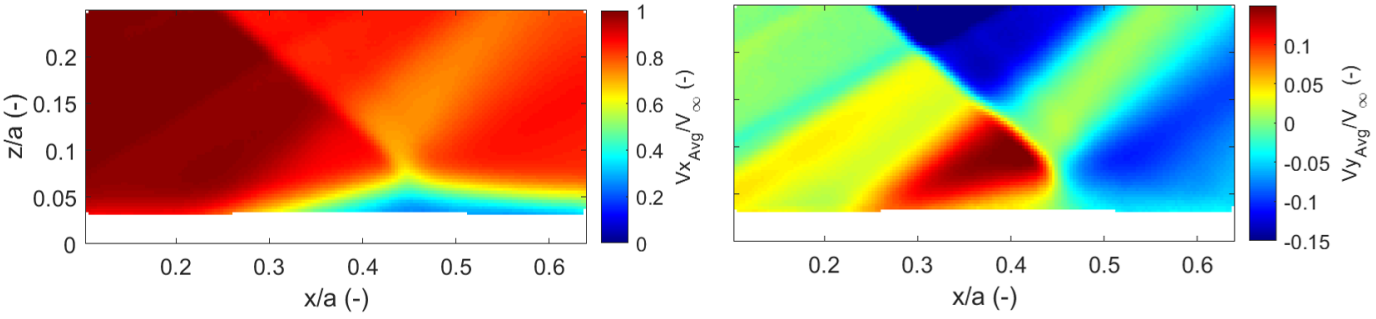

Figure 14. Average horizontal (left) and vertical (right) velocity fields with shock impingement.

unsteadiness are associated with the separated area and the reflected shockwave. It is interesting to notice that no increased values of the standard deviation are observed for the impinging shock or with the compression wave emanating from the leading edge of the panel. This second observation confirms that, at that location, the panel is always bent upwards (as the average and standard deviation of the displacement suggests), although some variations in the pressure wave strength are observable in the instantaneous images from Fig.16.

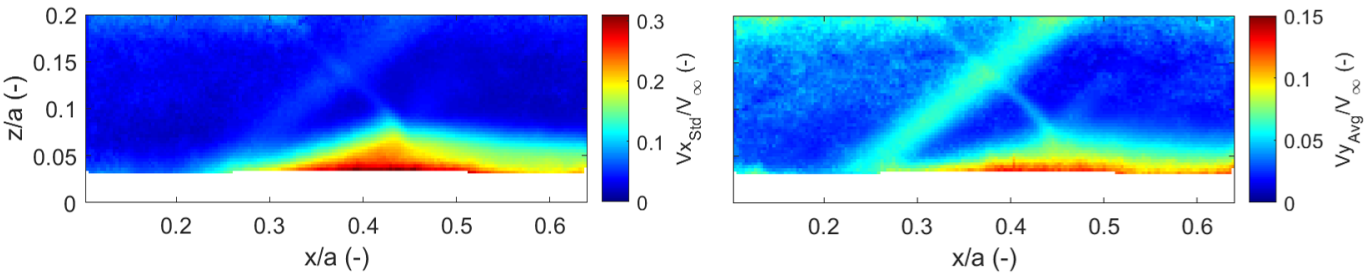

Figure 15. Standard deviation of horizontal (left) and vertical velocity component (right) with shock impingement.

4. Dynamic behavior

A sequence of the shock-induced fluid structure interaction taking place over the flexible thin panel with the (extrapolated) shock impingement point at 0.55a is shown in Fig.16, where the instantaneous horizontal velocity field is shown together with the vertical displacement field of the panel for different stages of a flutter cycle. The figure illustrates the capability of the set-up to capture the dynamics of both the flow field and the structural deformation. The flutter cycle described in Fig.16 has a duration of 2.4 ms and the four stages have a fixed time separation of 0.6 ms. The four time steps reveal that the panel is oscillating between a most upward (experienced in the first time step with maximum value of $z/h \approx 6$) and a most downward deformation (which is observable for $t = t_0 + 1.2\ ms$, with $z/h \approx -6$). In the two intermediate stages ($t = t_0 + 0.6\ ms$ and $t = t_0 + 1.8\ ms$) the panel deformation is smaller and shows a combination of upward and downward deflection along the plate. Near the leading edge, the panel has always a positive (upward) deformation, while near the trailing edge it is negative (downward) (as commented in Section 3). The reflected shockwave is clearly unsteady and oscillating with the panel motion, being in its most downstream position ($x/a \approx 0.3$) for $t = t_0 + 0.6\ ms$ and in the most upstream ($x/a \approx 0.2$) for $t = t_0 + 1.8\ ms$. In correspondence of the interaction between the impinging shockwave and the separated area, expansion waves are also observed. In addition to these classical SWBLI flow structures, the oblique compression wave emanating from the leading edge of the panel is once again observed, with its strength increasing when the deflection of the panel in proximity to the leading edge is larger. From the oscillation of the panel in time, it has been possible to describe its range of oscillation (in correspondence of the center line), both in presence and in absence of shock impingement (see Fig.17). With the dashed line, the average displacement of the panel is indicated, while with the two solid blue lines the maximum positive and negative displacement. The plots confirm the considerations previously taken into account for the average displacement fields. It is also interesting to note that for the shock impingement case the oscillation range of the panel ($-5 < z/h < 5$) is well above the value of the thickness of the panel ($z/h = \pm 1$), which is often referred to (see Dowell (1970)) as the threshold for the definition of the occurrence of supersonic panel flutter. Differently, for the case without shock impingement the panel oscillation is almost always below the limits imposed by ($z/h = \pm 1$), suggesting that for this configuration, panel flutter oscillations are not fully developed yet. A similar behavior was also observed by Beberniss et al.

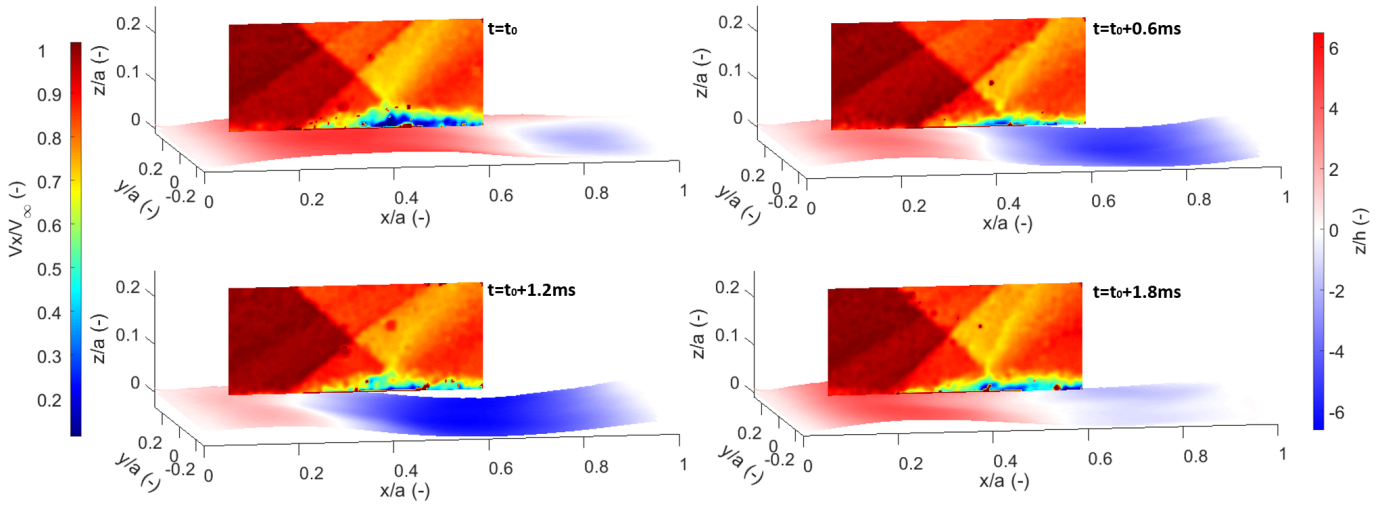

Figure 16. Simultaneous velocity and displacement field snapshots for a full flutter cycle.

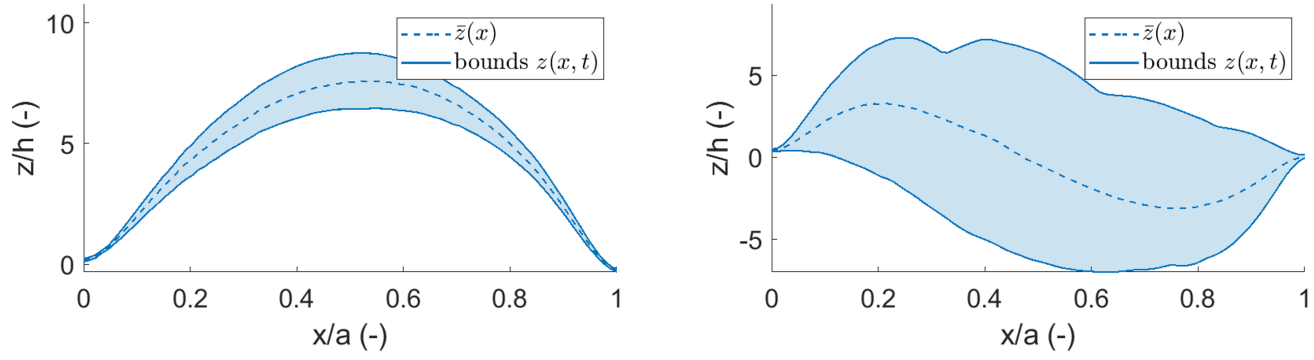

Figure 17. Mid-span (y/a=0) range of oscillation of the panel with (right) and without (left) shockwave impingement. The dashed lines indicate the average displacement profile.

(2011) where for a panel 0.635mm thick, a maximum displacement of around half of this thickness was observed. The results are however in disagreement with Beberniss et al. (2016) where a much more contained difference was observed between the shockwave and the non-shockwave case.
To substantiate the previous discussion, the panel displacement and its standard deviation are reported for both cases in Table 5 for the point of the panel with the largest standard deviation: $x/a = 0.5$ and $y/a = 0$ (which is also the centre of the panel). Similarly the average and the standard deviation of the reflected shockwave position X_{SWrefl}/a have also been included in the same table for both the rigid and the complaint panel. The reflected shockwave position has been tracked by looking at the minimum of the divergence field on a horizontal line with vertical coordinate $z/a = 0.1$. The range of oscillation of the shockwave (using as a proxy for this the standard deviation of the shockwave position, $\sigma(X_{SWrefl})$) is extended by roughly 80% in presence of the flexible panel.

Table 5. Comparison of flow and structure properties with and without shock impingement

	$\bar{z}/h$	$\sigma(z/h)$	$\bar{X}_{SWrefl}/a$	$\sigma(X_{SWrefl}/a)$
Flexible panel without shockwave	7.5	0.3	-	-
Flexible panel with shockwave	-0.3	2.1	0.32	0.026
Rigid panel with shockwave	-	-	0.33	0.014

4.1. Spectral analysis

A spectral analysis of the reflected shockwave and the panel displacement signals for all the cases studied is shown in Fig.18 in the form of a power spectral density (PSD), which has been obtained with the Welch method in this study. The PSD has been premultiplied for the frequency in order to obtain a physical quantity which is directly proportional to the energy of oscillation of the panel and of the reflected shockwave. To directly compare the spectral contents, all the PSDs have been normalised by the variance of the respective time signal.
For the shockwave case, the plot highlights a very similar behavior between the panel displacement and the reflected shockwave, with both signals exhibiting a main peak at 424 Hz, a secondary at 1354 Hz and a lower contribution at 576 Hz. The peak at 576 HZ is associated with a wind tunnel contribution, while the remaining two peaks with the flutter phenomenon.
Notwithstanding the good agreement between the spectral content of the two signals, for X_{SWrefl}/a the main frequency peaks are slightly less important than for the structure. This observation is due to an increase in relevance of the contributions at higher frequency for the SW signal.
For comparison, the premultiplied PSD of the reflected shockwave in presence of the rigid panel is also included in the same figure (which is normalized by the variance of the shockwave position for the flexible panel). Compared to the flexible panel, it is clear that for the rigid panel, the oscillation of the reflected shockwave is much less energetic and with the most relevant contributions for $200 < f < 350$ Hz. A similar distribution is also observed in van Oudheusden et al. (2011).
In absence of shockwave impingement a single dominant peak is observed at 730 Hz, while all the secondary peaks are more than one order of magnitude lower, in opposition with the shockwave case where two dominant peaks are present. This behavior is in agreement with the study of Visbal (2014) but is in disagreement with the results of Beberniss et al. (2011), who noticed a shift of the spectrum to higher frequencies when including the shockwave impingement.

5. Fluid-structure correlation

From the instantaneous images in Fig.16, it was observed that the reflected shockwave reaches its most upstream/downstream position in a different time step with respect to the stage in which the panel experiences its most upward/downward deflection. This information is quantitatively verified by the cross-correlation between the reflected shockwave position and the panel vertical

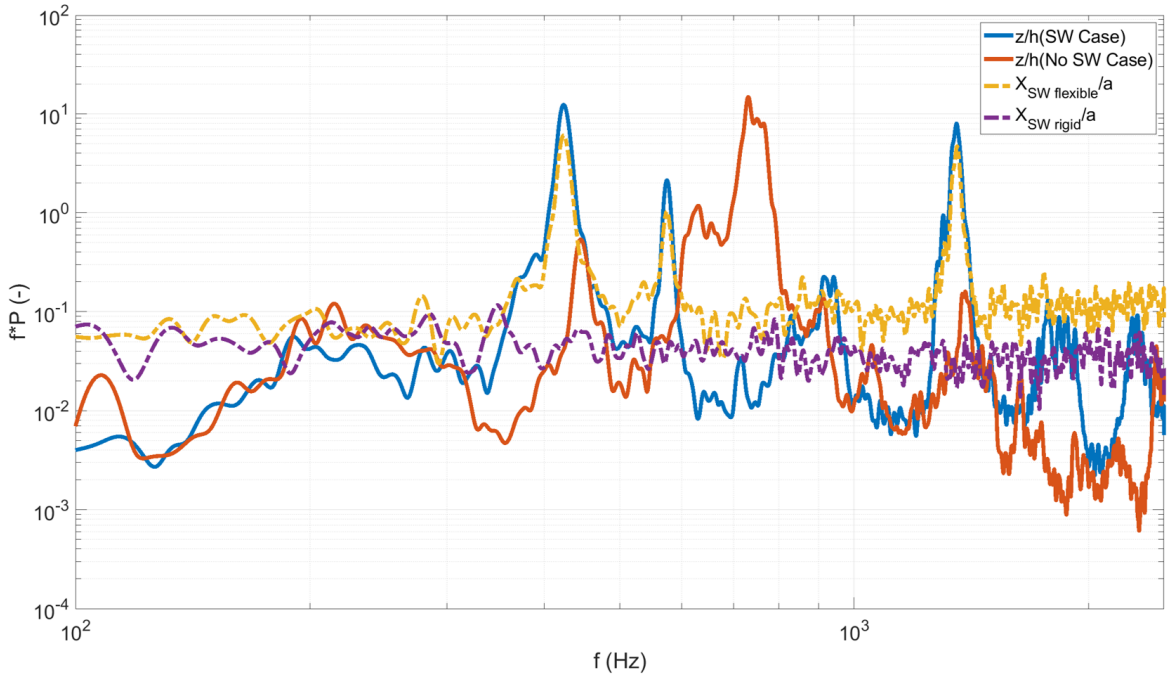

Figure 18. Pre-multiplied PSD of reflected shockwave position (for flexible and rigid panel) and panel displacement (with and without shock impingement).

displacement (see Fig.19). The latter has been considered in a point of the panel in the center of the range of oscillation of the reflected shockwave, thus in $x/a = 0.25, y/a = 0$. The plot reveals that the maximum correlation is obtained for a time delay $\tau = 0.6\ ms$, which is equal to one quarter of the flutter cycle (of roughly 2.4 ms). The periodical behavior of the cross-correlation corroborates the presence of a strong coupling between the panel movement and the reflected shockwave position and therefore, an exchange of energy between flow and structure, in view of the phase shift of 90 degrees between structural and shock motion.

The coupling between flow and structure not only concerns the reflected shockwave movement, but also the flow field as a whole. To better characterize this aspect, a cross-correlation between the same panel point ($x/a = 0.25, y/a = 0$) and the velocity field has been carried out. The results are shown in the form of a correlation map, showing in each point of the velocity field, the correlation value for zero time lag ($\rho(\tau = 0ms)$), for both the velocity components (see Fig.20).

The cross-correlation map indicates that there is a high degree of correlation ($|\rho| \approx 0.75$) between the panel displacement in $x/a = 0.25$ and the velocity field in the region in between the leading edge compression wave and the shockwave oscillation range $0 < x/a < 0.2$, although with an opposite sign for the two velocity components. The physical explanation for this correlation is that for a positive (upward) displacement of the panel, the leading edge compression wave increases in strength, and accordingly the vertical velocity increases (positive correlation) while the streamwise component decreases (negative correlation). On the other hand, a significant but lower correlation value ($|\rho| \approx 0.3$) is observable in the shock oscillation range for both velocity components.

Inspired by the results of Fig.19, the correlation maps are also determined (Fig.21) for a time

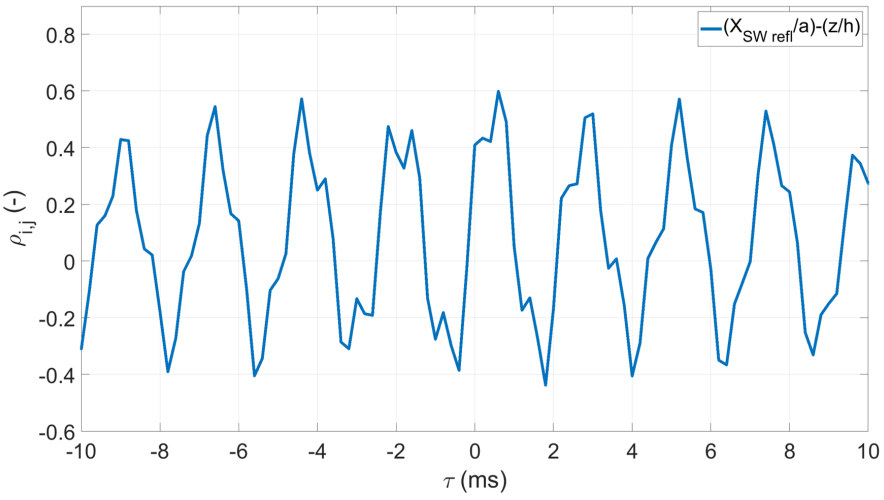

Figure 19. Cross-correlation between reflected shockwave and displacement of the structure (z/h) in x/a=0.25.

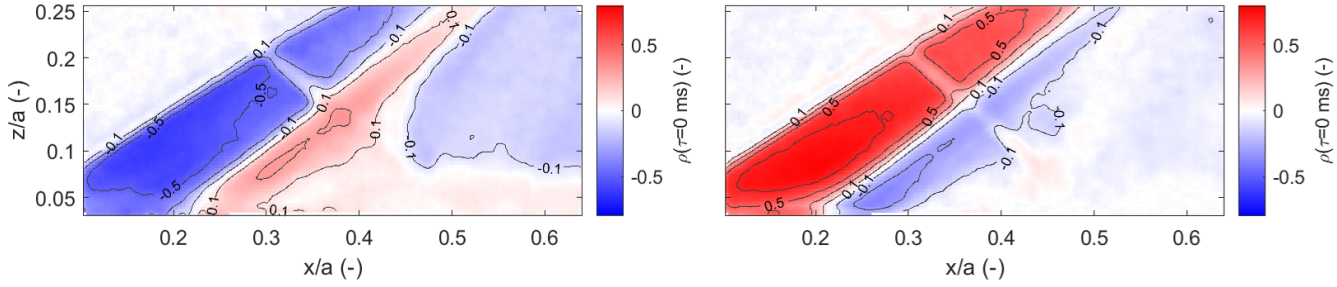

Figure 20. Cross-correlation between flow field (on the left V_x and on the right V_y) and displacement of the structure (z/h) in x/a=0.25 and y/a=0 for τ=0 ms in presence of shock impingement.

delay of 0.6 ms ($\rho(\tau = 0.6ms)$), revealing a relatively high correlation ($|\rho| \approx 0.6$) in the reflected shockwave oscillation range. The sign of the correlation is once again opposite for the two velocity components, since for more upstream shockwave positions there is an earlier (in terms of streamwise positions) decrease in the horizontal component of velocity and an earlier upward deflection of the streamlines.

For the horizontal velocity component (Fig.21, left), the regions of positive correlation are seen to extend to the entire interaction length and separated area, confirming the link between the reflected shockwave position and the separated area. For the vertical velocity component (Fig.21, right), downstream of the shockwave oscillation range, there is a further positive correlation area. This region is associated with the dynamics of the expansion waves originating from the interaction between the sonic line and the impinging shockwave, as sketched in Fig.1 (left). For the V_x correlation map, for $x/a > 0.45$ and $z/a > 0.1$ a region of high negative correlation is present, suggesting that for more downstream locations of the reflected shockwave, the value of the horizontal component of velocity is diminished.

Upstream of the reflected shockwave ($x/a < 0.2$) no relevant correlation between the panel and the flow is observed neither for the horizontal nor for the vertical component of velocity. This result was expected since the flow in this region is governed by the instantaneous local shape of the

panel, which is out of phase with the reference displacement point for the considered time delay.
For comparison, the cross-correlation map between the oscillation of the panel (again in $x/a = 0.25, y/a = 0$) and the flow field is also shown for the panel in absence of shockwave impingement. First of all, it is worth mentioning that for this case no delay between the flow and the structure is observed, thus the correlation map is only reported for $\tau = 0ms$.

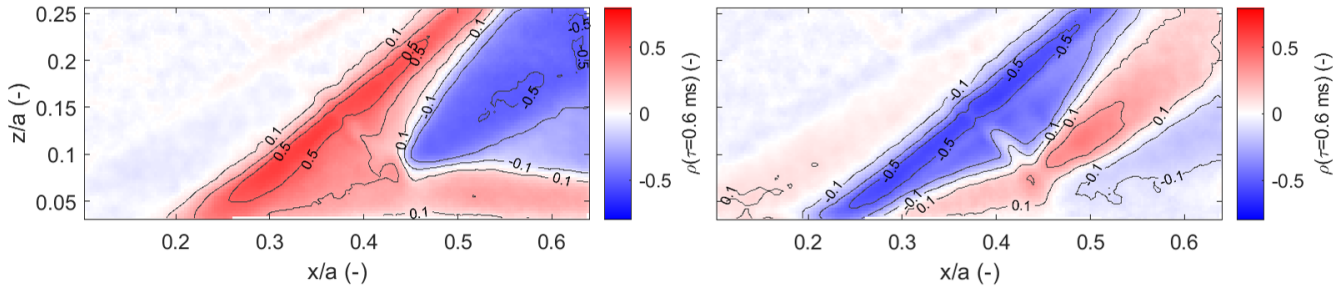

Figure 21. Cross-correlation between flow field (on the left V_x and on the right V_y) and displacement of the structure (z/h) in x/a=0.25 and y/a=0 for τ=0.6 ms in presence of shock impingement.

Downstream of the leading edge there is a region of modest correlation ($|\rho| \approx 0.3$, the sign of the correlation coefficient is again opposite for the two velocity component), in agreement with what was observed for the panel in presence of shockwave in the same region. However, in absence of shockwave, this region extends roughly up to the inflection point of the panel.
When comparing the correlation value between the shockwave and the non-shockwave case, lower peak values of correlation are obtained for the latter case. This behavior is supposed to be associated with the relevance of the respective panel oscillations, which, as shown in Table 5, are much more intense in presence of shock impingement.

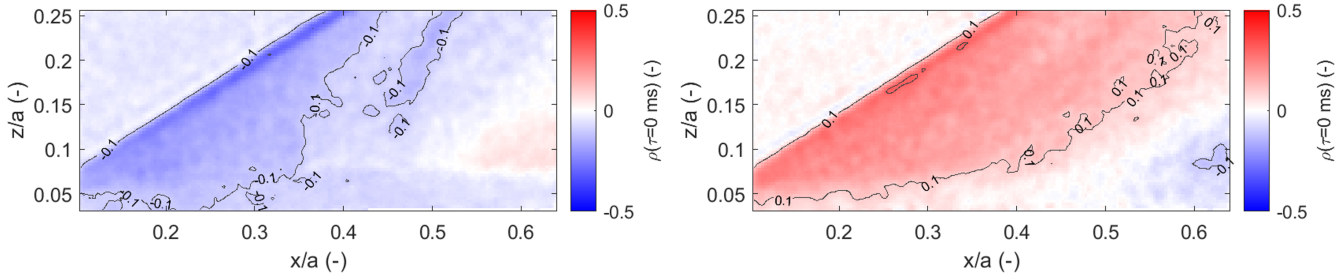

Figure 22. Cross-correlation between flow field (on the left V_x and on the right V_y) and displacement of the structure (z/h) in x/a=0.25 and y/a=0 for τ=0 ms in absence of shock impingement.

6. Conclusions

The reported findings show that an experimental simultaneous and time-resolved full-field analysis of structure and flow for classical and shock induced panel flutter is feasible with the proposed

techniques. This was the first investigation in which DIC and PIV have been employed in combination for studying this phenomenon, confirming the results obtained by Hortensius et al. (2018) for a similar application (although in this study neither the flow nor the structure were time resolved).

A good quality of the experimental data was achieved by optically separating the structure and flow measurements. The use of fluorescent paint, a dedicated blue LED illumination source and DIC highpass filters managed to noticeably reduce the interference of the PIV system on the DIC acquisitions. On the other hand, the use of a PIV bandpass filter helped to minimize the analogous DIC interference, but was found to be not very critical. Residual mutual interactions between the DIC and the PIV systems were quantified and considered negligible (Figs. 9, 10). Given the results obtained, this set-up demonstrated to be suitable for simultaneous PIV and DIC measurements.

The DIC measurements confirm the spanwise coherence of the (static and dynamic) displacement field (Figs.11, 13) as anticipated by the applied boundary conditions with free panel edges. This also justifies the use of planar PIV measurements in the centerline of the panel to characterize the flow for the current configuration. In applications where 3D structures are expected (as in the study of a panel clamped on all the four edges), however, a more elaborate (multiple-plane or volumetric) PIV approach may be required to properly characterize the flow field.

The DIC data showed that the average displacement field has a first bending mode shape for the non-shockwave case and a second bending mode shape (with an upwards deflection at the front part and a downwards deflection in the rear part) for the shockwave case. These shapes can be understood from the variation of pressure over the panel, which, for the shockwave case, increases in the downstream direction as induced by the impinging shockwave interaction, while the pressure is nearly constant in absence of shockwave.

For the shockwave case the oscillation amplitude of the panel is well beyond the commonly accepted flutter limit, with a maximum amplitude of $\Delta z/h \approx 10$ (Fig.17) . Differently, in absence of shockwave, the amplitude is in the order of the thickness of the panel, suggesting that in this case the flutter oscillations are not fully developed yet.

For the shockwave case, the oscillation dynamics of the panel and of the reflected shockwave are dominated by two contributions: the strongest at 424 Hz, and the second at 1354 Hz. The Strouhal number corresponding to the main contribution (f=424 Hz) of the shockwave oscillations (based on the mean interaction length) amounts to $St = 0.044$ and appears slightly shifted to higher St when compared to the values of the most relevant contributions ($St = 0.019 - 0.033$) obtained for a rigid wall surface (see also van Oudheusden et al. (2011)). Differently, for the non-shockwave case the dominant panel motion contribution is at 730 Hz, while secondary contributions are considerably less energetic. These results confirm that, as expected, the presence of the shockwave completely modifies the flutter response of the panel, not only changing the deformation shape and the amplitude of oscillation, but also the frequency of oscillation.

A cross-correlation between the panel movement and the complete flow field clarified that, for the shockwave case the region of the flow included between the leading edge compression wave and the reflected shockwave is directly in phase with the panel oscillation (Fig. 20). In contrast, the

velocity fluctuations in the shockwave oscillation range and in the region downstream of it, have a delay of 0.6 ms (one quarter of the flutter cycle) with respect to the panel motion (Fig.21). This lag is also qualitatively observed in the instantaneous images in Fig. 16 between the reflected shockwave position and the panel displacement. The correlation map in the isentropic portion of the flow field, as expected, resembles the map obtained for the non-shockwave case, where no delay is observable between the fluctuations of the flow and of the structure.
Although additional research is required, another aspect which could influence the flutter dynamics of both the configurations tested is the presence of the leading edge compression wave, whose variation in strength is associated with the local slope of the panel and hence is changing with the frequency of oscillation of the structure.

Acknowledgements

The authors acknowledge LaVison for having provided two LED lights for the experiments conducted in this study.
This work has been carried out as part of the project HOMER (Holistic Optical Metrology for Aero-Elastic Research), funded by the European Commission, program H2020 under Grant No. 769237.

References

Anderson, W. (1962). *Experiments on the Flutter of Flat and Slightly Curved Panels at Mach Number 2.81* (Tech. Rep.). s: California Institute of Technology and United States.

Babinsky, H., & Harvey, J. (2011). *Shock wave-boundary-layer interactions*. Cambridge University Press.

Beberniss, J., T., Spottswood, M., S., & Eason, J., T. (2011, 01). High-Speed Digital Image Correlation Measurements of Random Nonlinear Dynamic Response. , *6*.

Beberniss, J., T., Spottswood, M., S., Perez, A., R., & Eason, G., T. (2016, January). Nonlinear response of a thin panel in a multidiscipline environment: Part I-experimental results. In *Conference proceedings of the society for experimentalmechanics series* (Vol. 1, pp. 237–248).

Boyer, N., McNamara, J., Gaitonde, D., Barnes, C., & Visbal, M. (2018, 11). Features of shock-induced panel flutter in three-dimensional inviscid flow. *Journal of Fluids and Structures*, *83*, 490-506.

Brouwer, K. R., Perez, R., Beberniss, T. J., Spottswood, S. M., & Ehrhardt, D. A. (2021). Fluid-Structure Interaction on a Thin Panel Including Shock Impingement Effects. In *Aiaa scitech 2021 forum.*

Clemens, N. T., & Narayanaswamy, V. (2014). Low-frequency unsteadiness of shock wave/turbulent boundary layer interactions. *Annual Review of Fluid Mechanics*, *46*(1), 469-492.

Dowell, E. H. (1970). Panel flutter - A review of the aeroelastic stability of plates and shells. *AIAA Journal*, *8*(3), 385-399.

Dowell, E. H. (1975). *Aeroelasticity of plates and shells* [Book]. Noordhoff International Pub Leiden.

Dowell, E. H., & Bendiksen, O. (2010). Panel Flutter. In *Encyclopedia of aerospace engineering* (pp. 1–14). Encyclopedia of Aerospace Engineering.

Dowell, E. H., & Voss, H. M. (1965). Theoretical and experimental panel flutter studies in the Mach number range 1.0 to 5.0. *AIAA Journal*, *3*(12), 2292-2304.

Garelli, L., Paz, R., & Storti, M. (2010, 08). Fluid–structure interaction study of the start-up of a rocket engine nozzle. *Computers & Fluids*, *39*, 1208-1218.

Giepman, R. H. M., Schrijer, F. F. J., & van Oudheusden, B. W. (2018). A parametric study of laminar and transitional oblique shock wave reflections. *Journal of Fluid Mechanics*, *844*, 187–215.

Hortensius, R., Dutton, J. C., & Elliott, G. S. (2018). Simultaneous Flowfield and Surface-Deflection Measurements of an Axisymmetric Jet and Adjacent Surface. *AIAA Journal*, *56*(3), 917–932.

Humble, R., Scarano, F., & Oudheusden, B. (2007, 08). Particle image velocimetry measurements of a shock wave/turbulent boundary layer interaction. *Experiments in Fluids*, *43*, 173-183.

Kordes, E. E., Tuovila, W. J., & Guy, L. D. G. (1960). *Flutter Research on Skin Panels* (Tech. Rep. No. Report NASA-TN D451). National Aeronautics and Space Administration.

Mei, C., Abdel-Motagaly, K., & Chen, R. (1999, 10). Review of Nonlinear Panel Flutter at Supersonic and Hypersonic Speeds. *Applied Mechanics Reviews*, *52*(10), 321-332.

Pasquariello, V. (2018, 04). Analysis and Control of Shock-Wave / Turbulent Boundary-Layer Interactions on Rigid and FlexibleWalls. *Journal of Fluids and Structures*, *30*, 219-225.

Pasquariello, V., Hickel, S., Adams, N., Hammerl, G., Wall, W., Daub, D., … Gülhan, A. (2015). Coupled simulation of shock-wave/turbulent boundary-layer interaction over a flexible panel. In *6th european conference for aerospace sciences* (pp. 1–15).

Piponniau, S., Dussauge, J. P., Debiève, J. F., & Dupont, P. (2009). A simple model for low-frequency unsteadiness in shock-induced separation. *Journal of Fluid Mechanics*, *629*, 87–108.

Ragni, D., Schrijer, F. F. J., van Oudheusden, B. W., & Scarano, F. (2011, Jan 01). Particle tracer response across shocks measured by PIV. *Experiments in Fluids*, *50*(1), 53–64.

Schreyer, A.-M., Lasserre, J.-J., & Dupont, P. (2015, 09). Development of a Dual-PIV system for high-speed flow applications. *Experiments in Fluids*, *56*.

Sciacchitano, A., & Scarano, F. (2014, 07). Elimination of PIV light reflections via a temporal high pass filter. *Measurement Science and Technology*, *25*, 084009. doi:

Shinde, J., V., McNamara, J., J., & Gaitonde, V., D. (2019). Effect of Structural Parameters on Shock Wave Boundary Layer Induced Panel Flutter. In *Aiaa aviation 2019 forum.*

Shinde, J., V., McNamara, J., J., Gaitonde, V., D., Barnes, C., & Visbal, M. (2018, 06). Panel Flutter Induced by Transitional Shock Wave Boundary Layer Interaction. In *2018 fluid dynamics conference.*

Spottswood, M., S., Beberniss, J., T., Eason, G., T., Perez, A., R., Donbar, M., J., Ehrhardt, A., D., & Riley, B., Z. (2019). Exploring the response of a thin, flexible panel to shock-turbulent boundary-layer interactions. *Journal of Sound and Vibration*, *443*, 74-89.

Spottswood, M., S., Eason, T., & Beberniss, T. (2012). Influence of shock-boundary layer interactions on the dynamic response of a flexible panel. In *International conference on noise and vibration engineering (isma)* (pp. 603–616).

Sutton, M. A., Schreier, H. W., & Orteu, J. (2009). *Image correlation for shape, motion and deformation measurements: Basic concepts, theory and applications* [Book]. Springer US, New York.

Tripathi, A., Gustavsson, J., Shoele, K., & Kumar, R. (2021). Response of a Compliant Panel to Shock Boundary Layer Interaction at Mach 2. In *Aiaa scitech 2021 forum.*

van Oudheusden, B. W., Jöbsis, A. J. P., Scarano, F., & Souverein, L. J. (2011, September). Investigation of the unsteadiness of a shock-reflection interaction with time-resolved particle image velocimetry. *Shock Waves*, *21*(5), 397-409.

Visbal, M. (2012, 04). On the interaction of an oblique shock with a flexible panel. *Journal of Fluids and Structures*, *30*, 219-225.

Visbal, M. (2014). Viscous and inviscid interactions of an oblique shock with a flexible panel. *Journal of Fluids and Structures*, *48*, 27-45.

Willems, S., Gülhan, A., & Esser, B. (2013, January). Shock induced fluid-structure interaction on a flexible wall in supersonic turbulent flow. In Array (Ed.), *Eucass proceedings series - advances in aerospace sciences* (Vol. 5, pp. 285–308).

Zhang, P., & Porfiri, M. (2019). A combined digital image correlation/particle image velocimetry study of water-backed impact. *Composite Structures*, *224*, 111010.